The Astrophysical Journal Supplement Series, 183:261–277, 2009 August doi:10.1088/0067-0049/183/2/261

A MULTI-COLOR OPTICAL SURVEY OF THE ORION NEBULA CLUSTER. I. THE CATALOG

N. Da Rio[1,6], M. Robberto[2], D. R. Soderblom[2], N. Panagia[2,7,8], L. A. Hillenbrand[3], F. Palla[4], and K. Stassun[5]
[1] Max Planck Institut für Astronomie, Königstuhl 17, D-69117 Heidelberg, Germany; dario@mpia-hd.mpg.de
[2] Space Telescope Science Institute, 3700 San Martin Dr., Baltimore MD 21218, USA
[3] California Institute of Technology, 1200 East California Boulevard, 91125 Pasadena, CA, USA
[4] INAF—Osservatorio Astrofisico di Arcetri, Largo E. Fermi, 5 I-50125 Firenze, Italy
[5] Vanderbilt Univ., Department of Physics & Astronomy 6301 Stevenson Center Ln., Nashville, TN 37235, USA
Received 2009 April 6; accepted 2009 June 25; published 2009 July 23

ABSTRACT

We present *U*, *B*, *V*, *I* broadband, 6200 Å TiO mediumband, and Hα narrowband photometry of the Orion Nebula Cluster (ONC) obtained with the WFI imager at the ESO/MPI 2.2 telescope at La Silla Observatory. The nearly simultaneous observations cover the entire ONC in a field of about 34 × 34 arcmin. They enable us to determine stellar colors avoiding the additional scatter in the photometry induced by stellar variability typical of pre-main-sequence stars. We identify 2612 point-like sources in the *I* band; 58%, 43%, and 17% of them are also detected in *V*, *B*, and *U*, respectively. 1040 sources are identified in the Hα band. In this paper we present the observations, the calibration techniques adopted, and the resulting catalog. We show the derived color–magnitude diagram of the population and discuss the completeness of our photometry. We define a spectrophotometric TiO index that takes into account the fluxes in the *V*, *I*, and TiO bands. Comparing it with spectral types of ONC members in the literature, we find a correlation between the index and the spectral type valid for M-type stars, which is accurate to better than 1 spectral subclass for M3-M6 types and better than 2 spectral subclasses for M0-M2 types.. This allows us to newly classify 217 stars. In a similar way, we subtract from our Hα photometry the photospheric continuum at its wavelength, deriving calibrated line excess for the full sample. This represents the largest Hα star catalog obtained to date on the ONC. This data set enables a full re-analysis of the properties of the pre-main-sequence population in the Orion Nebula Cluster to be presented in an accompanying paper.

Key words: catalogs – open clusters and associations: individual (Orion Nebula Cluster) – stars: formation – stars: luminosity function, mass function – stars: pre-main sequence

Online-only material: color figures, machine-readable tables

1. INTRODUCTION

The Orion Nebula Cluster (ONC) plays a fundamental role in our understanding of star and planet formation, serving, along with the Pleiades and Hyades, as a fundamental calibrator and prototype for young stellar clusters. As the nearest site where the entire initial mass function (IMF), from $\simeq 25\ M_{\odot}$ down to 10 $M_{\rm Jup}$, can be studied with minimal foreground and background contamination (Jones & Walker 1988; Getman et al. 2005), it has been extensively investigated both at visible (Herbig & Terndrup 1986; Prosser et al. 1994; Hillenbrand 1997; Robberto et al. 2004) and near-IR (Hillenbrand et al. 1998; Hillenbrand & Carpenter 2000; Lucas & Roche 2000; Luhman et al. 2000; Slesnick et al. 2004) and mid-IR (Robberto et al. 2005; Smith et al. 2005). In particular, the ONC provides a unique opportunity for studying a stellar cluster at visible wavelengths that is rich (> 2000 members; Ali & Depoy 1995) and young ($\simeq$ 1 Myr; Hillenbrand 1997, hereafter H97). In most cases clusters of this age are embedded within their parental environment (Lada & Lada 2003), but in the case of the ONC the neutral material has been removed by the expansion of the H II region produced by the brightest cluster members, θ^1 Ori C in particular. By combining photometry and spectroscopy at visible wavelengths, it is possible to derive the extinction for each individual star, and therefore its absolute luminosity, radius, and a model-dependent mass and age (H97).

The Hubble Space Telescope Treasury Program on the Orion Nebula Cluster (HST GO-10246, PI M. Robberto) carried out multicolor visible photometry of the ONC with the highest possible spatial resolution and sensitivity in order to obtain the most accurate estimates of stellar parameters. The Hubble observations have been complemented by ancillary ground based observations, necessary because of the limitations of the *HST* data in regard to source saturation and variability. Source saturation with *HST* was unavoidable given the long exposures (approximately 340 s) used to reach high signal-to-noise on the faintest ONC members. This time is long enough that point sources in Orion brighter than $I \simeq 17.6$ mag saturate in the F775W and F850LP filters (*I*- and *z*-band equivalent) of the ACS/WFC. This roughly corresponds to masses at the hydrogen burning limit, assuming for the cluster a 1 Myr age and 414 pc distance (Menten et al. 2007). Concerning variability, the choreography of the HST Treasury Program observations did not enable a given field to be imaged in all filters in a single visit. Since most sources in the ONC present variability (Herbst et al. 2002), which is typical for T Tauri stars for both accretion processes (Classical T Tauri Stars, CTTS) and rotation of spotted surface stars (Weak-line T Tauri stars, WTTS), this adds a source of uncertainty, especially if the variability is wavelength dependent.

To supplement the *HST* observations, ground-based data have been taken simultaneously from CTIO (near-infrared) and La Silla (optical) on two nights in 2005 January. The near-infrared

[6] Member of IMPRS for Astronomy & Cosmic Physics at the University of Heidelberg.
[7] INAF-CT Osservatorio Astrofisico di Catania, Via S.Sofia 79, I-95123 Catania, Italy.
[8] Supernova Ltd, OYV #131, Northsound Road, Virgin Gorda, British Virgin Islands.

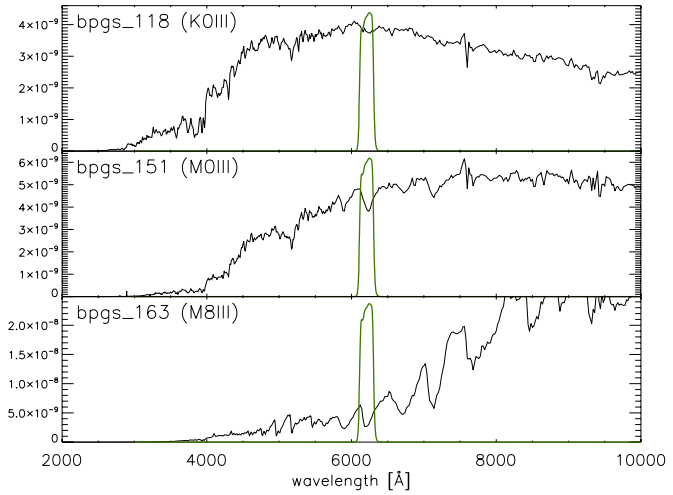

Figure 1. Mediumband MB#620/17_ESO866 filter response curve plotted over three standard spectra of giant stars (luminosity class III) of the Bruzual–Persson–Gunn–Striker catalog: *46LMI* (spectral type K0), *HD116870* (M0), and *Z Cyg* (M8). The TiO band mapped by this filter is stronger for late spectral types.

(A color version of this figure is available in the online journal.)

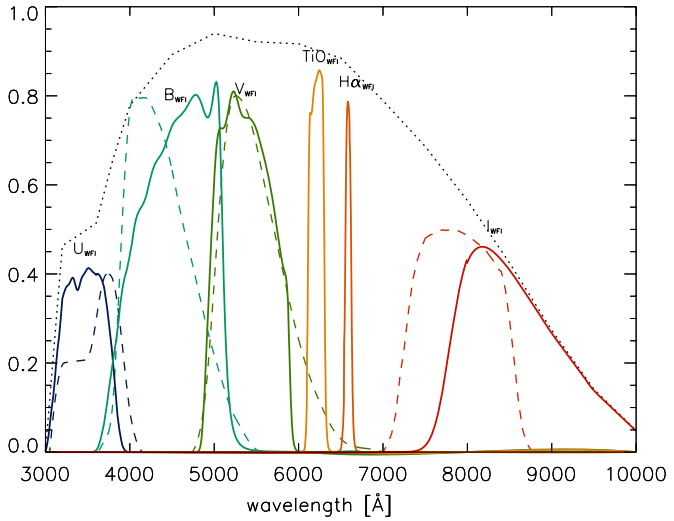

Figure 2. Band profiles for the six filters used in our observations (solid curves). The upper dotted line in black traces the CCD quantum efficiency; dashed lines in color represent the standard Johnson *U*, *B*, *V*, and Cousins I_C bands. The ESO879 *I* band is centered at a significantly higher wavelength (∼8269 Å) than its Cousins counterpart.

(A color version of this figure is available in the online journal.)

J, *H*, and *K* data and results are presented in M. Robberto et al. (2009, in preparation), and their discussion in not an aim of this work. At La Silla, we used the Wide Field Imager (WFI) at the ESO-MPI 2.2 m telescope to image the same field in the *U*, *B*, *V*, and *I* bands, as well as in the Hα line and in a medium resolution filter at 6200 Å. For stars earlier than late K type, this filter samples the R-band in a region free from major nebular lines, whereas for M-type stars and substellar objects it turns out be centered on a TiO absorption feature whose strength depends on the spectral type, growing toward the latest M types. In Figure 1 we show an example of three standard spectra taken from the Bruzual–Persson–Gunn–Striker spectral atlas (Gunn & Stryker 1983), showing how the absorption band coincides with the filter profile. A photometric study which includes narrowband measurements at 6200 Å might therefore be helpful for constraining the spectral type of cool stars, as well as disentangling the temperature-reddening degeneracy in the observed broadband colors. In what concerns the Hα photometry, it can be used to assess membership, and derive mass accretion rates through an absolute estimate of the accretion luminosity.

In this paper we present the WFI data set. We describe the observations in Section 2, their reduction and calibration in Section 3, and results in Section 4. In particular, the photometric catalog, the corresponding color–magnitude diagram, and the completeness of our sample are described in Section 4.1. In Section 4.2 we focus on the 6200 Å mediumband photometry, from which we derive a spectrophotometric index correlated with the spectral type. In Section 4.3 we derive the line excesses in the Hα line. We summarize this work in Section 5. This data set allows us to revisit our current understanding of the ONC. This will be discussed in an accompanying paper (N. Da Rio et al. 2009, in preparation).

2. OBSERVATIONS

The Wide Field Imager (WFI) is a focal reducer-type camera mounted at the Cassegrain focus of the 2.2-m MPG/ESO telescope at La Silla. The camera features an array of 8 2 k × 4 k pixel CCDs, arranged in a 4 × 2 mosaic. The optics deliver a field of view of 34 × 33 arcmin with 0.238 arcsec per pixel scale. The WFI CCDs have a typical read noise of 4.5 e^- pix^{-1} and a gain of 2.2 e^- ADU^{-1}.

We selected the ESO877, ESO878, ESO843, and ESO879 broadband filters, roughly corresponding to the standard *U*, *B*, *V*, and *I* bands (note that the ESO879 *I* band is centered at a wavelength higher than the standard I_C band; see Figure 2), and the mediumband MB#620/17_ESO866 and narrowband NB#Halpha/7_ESO856 filters. We refer in this work to the MB#620/17 filter as the *TiO band*.

Our target field was observed in service observing mode on the nights of 2005 January 1 and 2 (hereafter indicated as Night A and Night B, respectively). The same observing strategy was adopted on both nights: for each filter we took five dithered exposures of 280 s ("Deep") and 30 s ("Medium"), plus one single 3 s short exposure ("Short"). The five dithered exposures made it possible to eliminate the gaps between CCDs in the final mosaics, whereas the different exposure times increase the dynamic range of measured magnitudes. The final size of the mosaics, trimmed to the largest common area, is approximately 35 × 34 arcmin. Absolute photometric calibration was obtained by comparison with the Landolt SA 98 field (Landolt 1992), observed twice each night at low and high air mass. The average seeing was better in Night A than in Night B (respectively 1.″2 and 1.″8).

3. DATA REDUCTION

3.1. Images and Source Catalogue

The data were reduced using a version of *alambic*, the ESO/MVM (Multi-Vision Model) image reduction system (Vandame 2004) as part of the EIS project for basic reduction of imaging data for a number of ESO imaging instruments. To speed up the data processing, we installed the package and ran the pipeline parallel version on a server cluster at the Space Telescope Science Institute.

The package automatically performs all the common image reduction steps: removal of instrument effects (bias removal,

flat field normalization), computation and removal of fringing (only present in *I*-band exposures), bad-pixel-map creation, and normalization of gain levels between different CCD chips.

Alambic also performs both relative and absolute astrometric calibration and distortion correction of the images to enable alignment and stacking of dithered frames. This step is achieved by retrieving an astrometric reference catalog, by default the GSC2 catalog, from the ESO archive. Since the GSC2 catalog turns out to be deficient in the Orion Nebula region, we used instead the Two Micron All Sky Survey (2MASS) *J*-band catalog, which therefore represents our absolute astrometric standard. The near-IR 2MASS catalog does not trace well the distribution of sources at our shortest wavelengths; thus, an iterative process has been carried out: the *J*-band reference catalog has been used for absolute astrometric calibration of the TiO and *I* bands. For the *V* band we bootstrapped from these two bands, extracting from the TiO and *I* calibrated images a secondary photometric catalog; the resulting *V* catalog was then used to perform astrometric calibration of *B*-band images, and finally the *B* catalog was used for the *U* exposures. The final coordinates of bright blue sources detectable in all images have been checked to assess the accuracy of the procedure, which typically provides coordinates that agree to within one pixel between different bands. A better astrometric calibration is not needed for our purposes, considering that the average FWHM for the point-spread function (PSF) in the data is ~ 1.5 arcsec, or 6 pixels. After astrometric calibration, all final images with the same filter and exposure time have been co-added using SWarp, a package included in the TERAPIX package (Bertin et al. 2002).

For the four U, B, V, I broadbands PSF photometry has been performed using the Daophot II package (Stetson 1987) on all the broadband filter images. Unlike aperture photometry, which we used instead for the narrowband filters, PSF photometry resolves and measures with good accuracy the luminosity of stars in highly crowded areas, such as the Trapezium region. We computed the PSF function for every image, using a set of reference stars located over the entire frame, and then refined this with an iterative sigma-clipping algorithm that rejected the candidates with excessive χ^2. PSF fitting was then performed on all the sources extracted with peak above 3σ of the local mean sky background, evaluated for every image using the SExtractor tool (Bertin et al. 2002). We did not attempt to recover saturated sources, relying instead on the frames with shorter exposure times; only a small number of stars turned out to be saturated even in the 3 s exposures too, and are therefore not present in our final catalog.

For each field and filter, we merged the photometric catalogs obtained with the different exposure times on the basis of the absolute positions of the sources, using the DAOMASTER package (Stetson 1987). Systematic differences in magnitude between different frames (mostly due to air-mass variations) have been corrected assuming that the fundamental instrumental magnitude is the one measured on the short (3 s) exposures. The instrumental magnitudes of stars well measured in different images have been averaged.

For every filter and exposure time we eventually kept only the sources detected in both nights in order to reduce contamination from spurious detections, which turns out to be not negligible due to the deep threshold (3σ) chosen for source identification. We have matched the photometry in the six bands using again DAOMASTER, keeping only those that present a counterpart in two adjacent bands, starting from the reddest ones (i.e., sources found in *V* and *I*; then *B*, *V*, and *I*; then *U*, *B*, *V*, and *I*). This is because we expect the observed spectral energy distributions (SEDs) to increase with wavelength in the visible range for all the faint, red end of the population; in other words, faint sources may be present only at the longer wavelengths, remaining invisible at the shortest ones; on the other hand, bright sources have been detected in all filters, if not saturated. For the Hα and TiO (6200 Å) bands we performed aperture photometry, evaluating and correcting the aperture correction to be applied using the brightest sources in the sample. These data have been first independently matched, keeping only stars detected in both filters on both nights to eliminate the eventual spurious detection, and afterward have been measured and matched to the broadband catalog.

To ensure that our catalog is free from any additional spurious detections, we checked our final list of bona fide candidates by visually inspecting their appearance in every filter. The data relative to the two nights have not been merged; thus in the final catalog the photometry of each source has two entries. However, given the better sky conditions in Night A, we will concentrate our analysis to the data taken on this night.

3.2. Absolute Calibration

3.2.1. Broadband Photometry

Traditionally, the absolute calibration of optical photometry is achieved by determining the transformation between the instrumental and the Johnson–Cousins photometric systems. This method assumes a linear or polynomial dependence of the magnitude offset for a given band as a function of a color index. This relation should be derived from a number of standard stars observed under the same conditions. In this work we chose not to perform a color correction, but instead we define a new photometric system based on the actual throughput of our passbands. This turns out to be an advantage, considering that there are several sources of uncertainty regarding the color correction to be applied. The main reasons of concern are the following.

First, our set of observed pre-main-sequence (PMS) stars includes some with very high color indices, up to $V - I \sim 6$. This is due to the combination of low $T_{\rm eff}$ for the low mass objects and high A_V in the region. The standard stars observed in the field SA98 reach only color terms up to $V - I \simeq 2$. There is no reason to assume that the linear transformation extracted from these standard stars can be extrapolated to the very red PMS stars. In fact, typical standard stars do not provide any information about the color corrections at extremely red color.

Second, in general the strengths of spectrum features that characterize stars of different $T_{\rm eff}$ depends on several other parameters besides temperature, such as surface gravity and metallicity. In continuum-dominated SEDs, as for early-type stars, these parameters have little effect in the computation of the integrated colors, but for late-type stars, whose SEDs are increasingly dominated by broad, strong molecular absorption bands (mostly TiO and VO), magnitudes are sensitive to changes in the strength of these features resulting from differences in the physical parameters, and so are the colors and color corrections. Thus, besides our lack of knowledge about the shape of the color corrections for red objects (see above), these corrections are not unique for all the ONC members.

In order to assess the first point we performed a test extracting synthetic photometry from a set of stellar atmosphere models. We used the NEXTGEN models (Hauschildt et al. 1999),

choosing a set of spectra with $2600 \leqslant T_{\rm eff} \leqslant 8200$ K and $\log g = 3.5$.[9] Synthetic photometry has been derived using the GENSYNPHOT software included in the CHORIZOS package (Maíz-Apellániz 2004). We defined the WFI bands by multiplying the filter transmissions by the CCD quantum efficiency curves, quantities that are well known for the WFI instrument, and then computed the zero points of this newly defined VEGAMAG photometric system using the calibrated Vega spectrum distributed with the CHORIZOS package. The measured instrumental magnitudes, therefore, are already expressed in this photometric system except for constant zero points depending on the observing conditions. These offsets in fact coincide with the zero points derived from standard field observations according to the standard method for photometric calibration (when we consider the color term relative to the calibrated magnitudes of the standard stars). This fact is clear considering the standard transformation, for instance, to calibrate an instrumental B-band photometry. We have that $(B - B_{\rm WFI,Ins}) = ZP + CC \cdot (B - V)$, where $B_{\rm WFI,Ins}$ is corrected in order to be valid for the air mass of the science observation in this band, from the two repetitions of standard field observations which were originally taken at low and high air mass each night. The intercept $(B - V) = 0$ corresponds to a Vega-type star, and in this case we have that $B - B_{\rm WFI,Ins} = ZP$. Furthermore, in the VegaMag convention, all the colors must be zero for a Vega-type star, so $(B - B_{\rm WFI,VegaMag}) = 0$. From these two expressions, finally, $(B_{\rm WFI,VegaMag} - B_{\rm WFI,Ins}) = ZP$. The same method used for all the bands results in an absolute calibration of the photometry in the instrumental-VegaMag photometric system.

We then computed the synthetic magnitudes for stars with different $T_{\rm eff}$ (i.e., different colors) in both the instrumental and the Johnson-Cousins photometric systems, determining the color-correction relations. The results are shown in Figure 3 for the four broadband filters used. In every case the nonlinearity of these transformations is evident for high color terms; this effect affects dramatically the B band, with shifts up to few tenths of magnitude from the linear color-correction relation at high $B-V$.

While, in principle, it could be possible to apply the simulated color-correction law, these are sensitive not only to the stellar parameters, but also to the accuracy of the synthetic atmosphere models. Unfortunately the uncertainties present in all these grids, especially in the temperature range of the M-type stars, are still limiting factors for an accurate evaluation of the integrated colors (see Baraffe et al. 1998). Therefore, it is clear that keeping our catalog in the instrumental system removes most of the uncertainties related to the absolute photometric calibration and, as we are going to show in a second paper within this project, preserves the capability of studying the stellar parameters through direct comparison of the observations with theoretical models. Our treatment of the color effects at high color terms and low surface gravity (in both band transformations and bolometric correction) represents a major improvement over the H97 analysis.

3.2.2. Narrowband Photometry

Due to the lack of standard star reference photometry in the two narrowbands in our data set (the 6200 Å TiO band and the Hα band), a traditional zero-point calibration approach cannot be followed; thus, we calibrated these data as follows.

[9] This value of $\log g$ is approximately one tenth of the solar value, and, according to the tables of H97, is a good enough approximation along all the temperature ranges in the ONC.

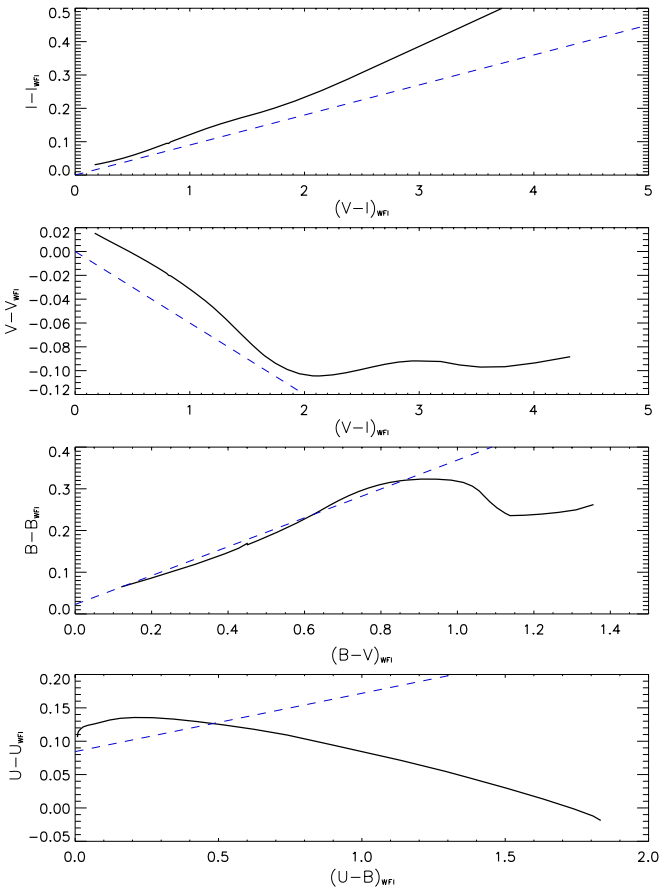

Figure 3. Transformations between the WFI instrumental photometric system and the standard Johnson–Cousins system. The dashed line refers to the linear relations obtained from standard field observation (extrapolating the filters color terms comparing the observed colors with tabulated standard magnitudes spanning a more limited range in color); the solid line is the result of synthetic photometry using NEXTGEN models with $\log g = 3.5$ and $2600 \leqslant T_{\rm eff} \leqslant 8200$ K. B and U bands show high differences due to nonlinearity of the color correction.

(A color version of this figure is available in the online journal.)

First, the photometry of the two nights has been cross-calibrated, matching identical stars and determining the global average offset of night B versus night A; this step allows us to clean the sample from spurious detections. Then the magnitudes have been converted to units of flux (counts s^{-1}). We computed the ratio between the actual efficiencies (measured ADU/flux) between the TiO band and the Hα filter, taking into account the differences in the filter passbands, the quantum efficiency $QE(\nu)$, of the WFI CCDs, air mass—deriving the atmospheric extinction at 6200 Å linearly from the ones measured in V and I—and photon energy. In this way we derived a priori that, considering the observations of night A, a constant flux observed in both filters (in terms of Jy) corresponds to a number of ADUs in the Hα images $\sim$2.70 lower that in the TiO images. Therefore, correcting for this factor, we *relatively* calibrate the Hα photometry on the TiO one. The subsequent absolute calibration of the latter, therefore, calibrates the Hα as well.

The problem is therefore to find the magnitude offset to apply to the TiO photometry in order to express our data in standard VegaMag. By definition this offset is such that a for a Vega-type star all the colors are zero, for instance $(V_{\rm WFI} - {\rm TiO}) = 0$ or $({\rm TiO} - I_{\rm WFI}) = 0$. Unfortunately our sample lacks a significant number of such objects, requiring us to use stars of later type to improve the precision of the calibration. If we consider

Table 1
Central Wavelength and FWHM of the WFI Filters Used

Band	λ_{cen} (Å)	FWHM (Å)
U	3404	732
B	4511	1335
V	5395	893
I	8269	2030
TiO	6208	194
Hα	6588	74

the most abundant M-type stars in our catalog, however, the behavior of the measured flux in TiO is strongly affected by the absorption feature shown in Figure 1. We consider therefore the intermediate temperature stars (G and early K spectral types), isolated in our sample by matching our photometric catalog with the spectroscopy of Hillenbrand (1997). A first-order estimate of the calibration to be applied to the TiO photometry could be to impose that, for these stars, the magnitude at 6200 nm is equal to the linear interpolation of the *V* and *I* magnitudes, assumed at a wavelength equal to the average wavelength of the band profiles (see Table 1). We investigate the correctness of this assumption using synthetic photometry on a grid of atmosphere models. We consider the NextGen (Hauschildt et al. 1999) grid, for solar metallicity and surface gravity $\log(g/g_{\odot}) = 3.5$, an average value for PMS stars. In the temperature range we selected—for which the uncertainty of the theoretical spectra is negligible (Baraffe et al. 1998)—the models predict that the TiO magnitude is on constantly 0.17 mag brighter than the assumed linear interpolation, and therefore we applied this offset in order to calibrate the TiO photometry. Once the photometry in VegaMag is calibrated, we are able to express it into physical flux, calculating the zero point of the band of 3.175150×10^6 mJy by means of integration of a reference Vega spectrum

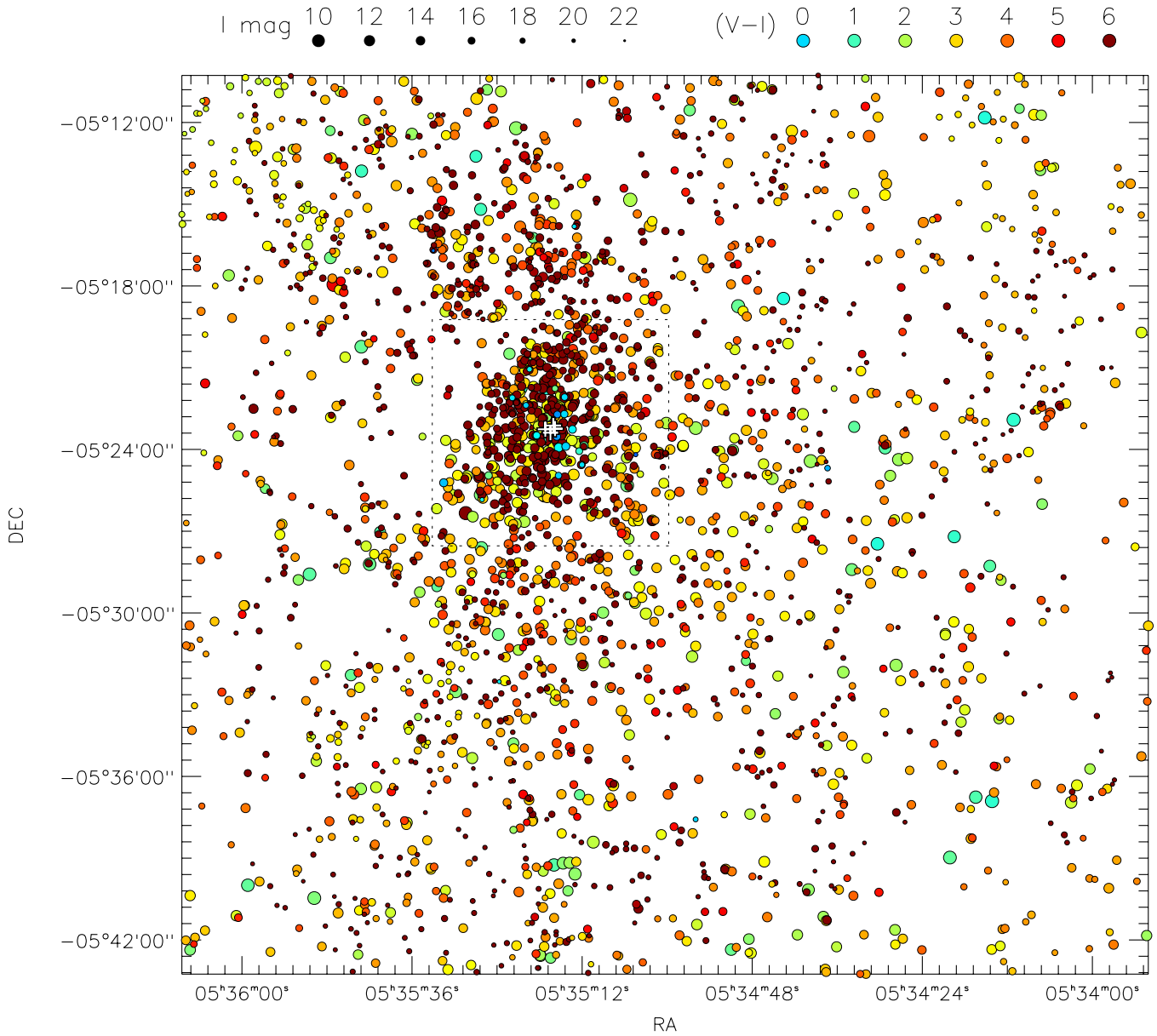

Figure 4. Point-like sources selected in the final catalogue with at least *V* and *I* magnitude detected for both night A and B. The size of the dots increases with *I* magnitude, and the colors represent the *V*−*I* values as shown in the legend. The position of the four stars of the Trapezium cluster is shown with crosses. The dotted contour delimits the central area of 1 pc of size centered on the star $\theta_1 c$ of the trapezium cluster. The zoomed spatial distribution within such a region is shown in Figure 5.

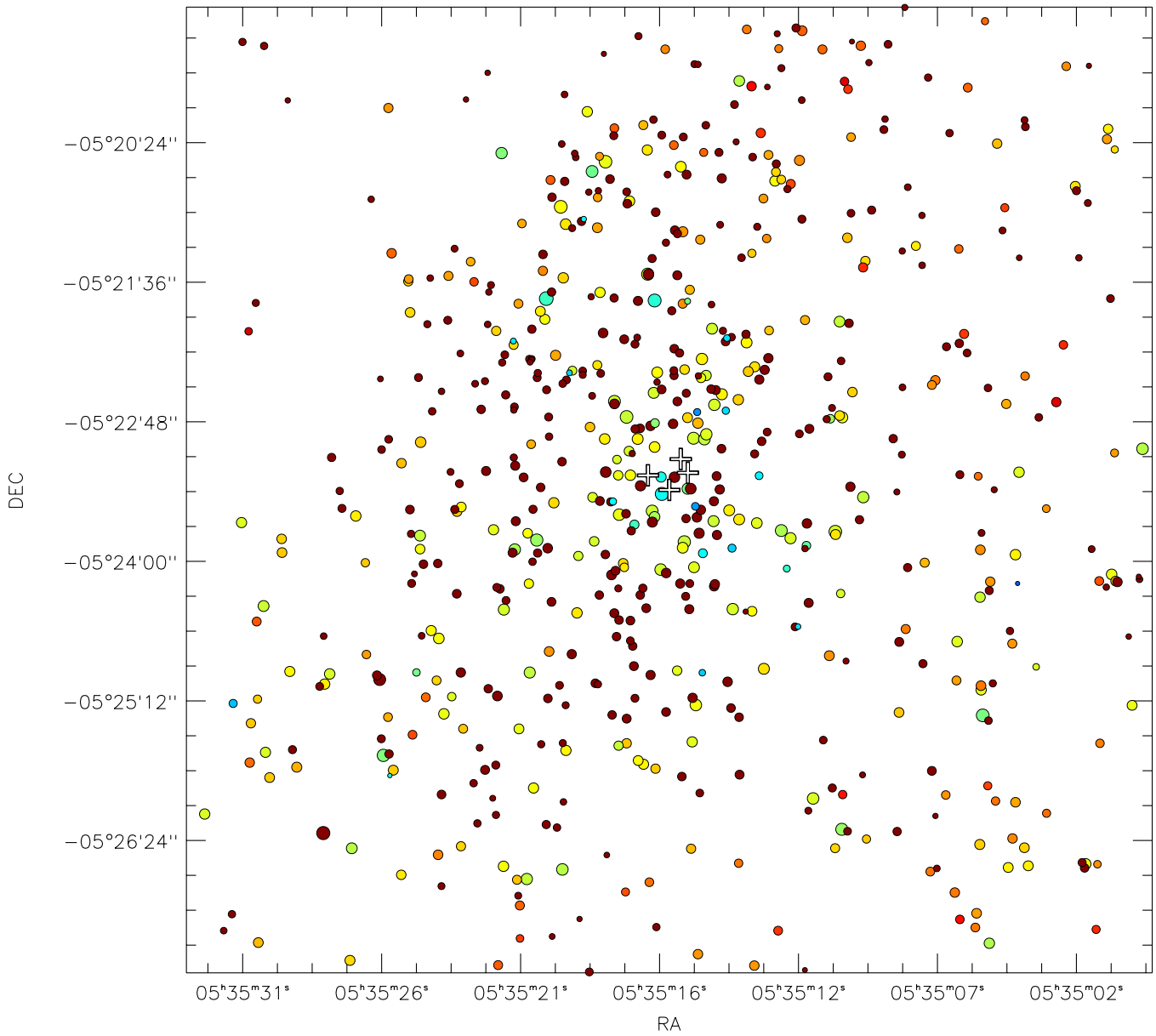

Figure 5. Same as Figure 4, for the inner area (1 pc of size) centered on the star $\theta_1 c$.

using the *STSDAS Synphot* software. Given that we calibrate the Hα photometry in units of flux relatively to the TiO, the same zero point, as explained above, is therefore the same also for the absolute calibration of the Hα photometry.

4. RESULTS

4.1. The Source Catalog

The final catalog includes 2621 point-like sources detected in the *I* band, 1523 of which have both *V* and *I* magnitudes, 1134 also *B* magnitudes, and 431 have *U* magnitudes. Narrowband photometry is available for 1040 stars. As mentioned above, the catalog itself provides for each star two distinct photometric values for nights A and B, respectively; however, given the poor sky conditions of night B, we present only the results from the observations during the first night.

In Figure 4 we present the distribution on the sky of the detected sources. The general structure of the cluster, elongated in the north–south direction as already described in Hillenbrand & Hartmann (1998), is evident. In this figure we also highlight different luminosities with the dot size and the $(V - I)$ indexes with colors. Figure 5 is the same as Figure 4, but for the inner region of 1 pc of size centered on the trapezium cluster.

Figure 6(a) shows the photometric errors as a function of luminosities for the UBVI+TiO filters. The visible multiple trends in the distribution of photometric errors are due to the superposition of deep, medium and short exposures. Bright stars are likely to be measured only in short exposures being saturated in the long ones, and their photometric error turns out relatively high. Figure 6(b) presents the observed luminosity functions (LFs) in the five bands.

In Figure 7 we present the color–magnitude diagram for the four broadband filters. We use different symbols for the stars having all the four broadband magnitudes are available, only *B*, *V*, and *I*, or only *V* and *I*. Given the red colors of

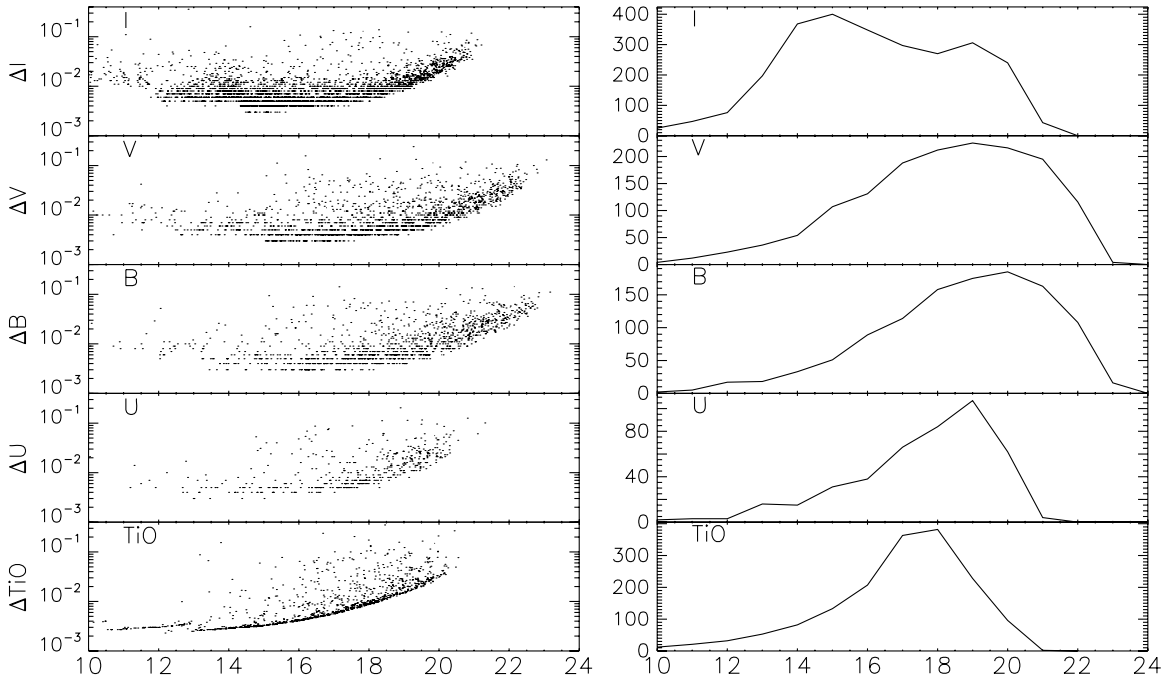

Figure 6. Left panel: photometric errors for the five bands observed. Right panel: LFs. The double peak in the *I* band is reasonable due to contamination by background stars.

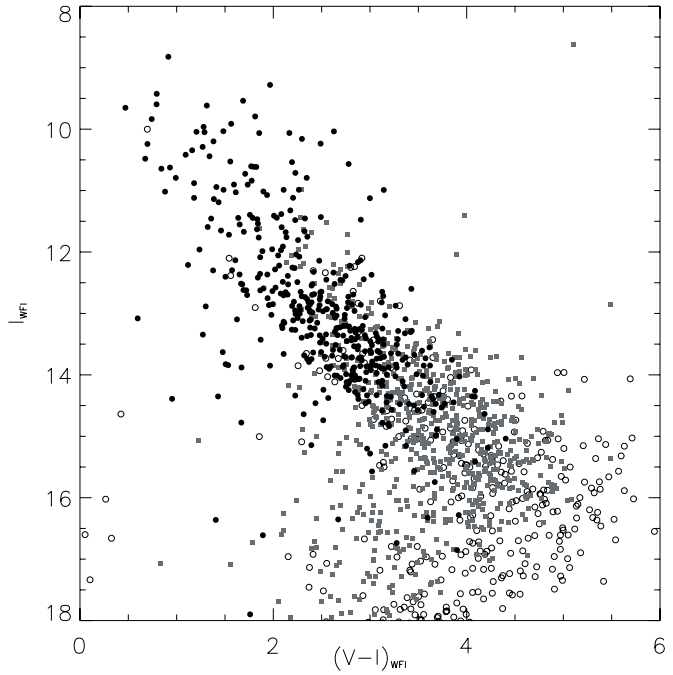

Figure 7. Instrumental color–magnitude diagram for the sources present in our catalog: filled circles are objects with all *U*, *B*, *V*, and *I* measures, squares are sources lacking *U*, and open circles are objects with only *V* and *I* magnitudes.

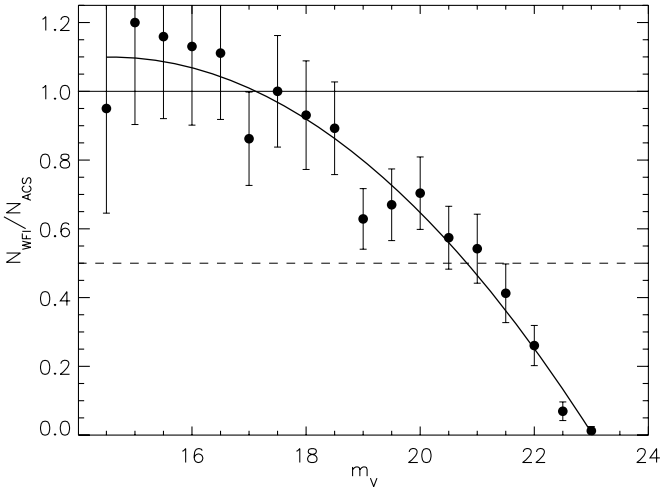

Figure 8. Completeness function for the *V* band. Dots represent the measure ratio between the number of sources counted in bins spaced 0.5 magnitudes in the WFI and the *HST*/ACS catalog respectively, considering only the common FOV of the two surveys. A polynomial fit of the second order is overlaid. The apparent systematic completeness greater than unity in the bright end is due to source saturation of the ACS imaging.

the ONC members, the faint stars lack signal at the shorter wavelengths.

We estimated the completeness limit of our survey, comparing our LFs in the *V* band with the one derived from the *HST*/ACS catalog (M. Robberto et al. 2009, in preparation) in the *V*-equivalent filter F555W. The *HST* survey is characterized by a considerably fainter detection limit. In order to allow for a consistent comparison, we considered only sources present in the common field of view. This, which is about 55% of the $\sim$ 1100 arcmin^2 total WFI FOV and contains about 70% of the WFI sources we detected, is wide enough to be well representative of the whole observed area, covering both the central part of the cluster, more affected by crowding, and the loose periphery. The ratio between LF counts, as a function of the *V* magnitude, directly provides our completeness function in this band. It is shown in Figure 8. At the bright end of the distribution the deep ACS catalog is deficient of sources with respect to WFI, due to saturation and to the presence of nonstellar sources (e.g., proplyds or circumstellar halos) which may contaminate our lower resolution of ground based catalog. At the faint end, the ratio of sources detected with WFI to $\sim$50% at $V \simeq 20.8$, which we therefore consider as representative of our completeness limit for the source detected in both *V* and *I* bands.

Table 2
WFI Photometric Catalog Relative to Night A Observations

ID	R.A. (J2000.0)	Decl. (J2000.0)	U	ΔU	B	ΔB	V	ΔV	TiO	ΔTiO	I	ΔI	H97 ID
0001	05 35 47.01	−05 17 56.9	...	...	16.093	0.004	13.728	0.004	12.097	0.003	8.626	0.027	992
0002	05 35 20.71	−05 21 44.4	9.886	0.008	10.041	0.009	9.736	0.008	9.540	0.004	8.822	0.021	660
0003	05 35 05.20	−05 14 50.3	13.260	0.007	12.141	0.011	11.246	0.017	10.535	0.003	9.280	0.036	260
0004	05 34 14.16	−05 36 54.1	11.081	0.005	10.697	0.009	10.219	0.010	9.929	0.004	9.425	0.016	...
0005	05 35 21.31	−05 12 12.7	13.057	0.004	12.043	0.052	11.225	0.015	10.646	0.003	9.538	0.018	670
0006	05 35 28.41	−05 26 20.1	...	...	...	...	...	...	9.601	0.004	9.552	0.016	831
0007	05 34 11.11	−05 22 54.6	11.199	0.014	10.900	0.008	10.388	0.010	10.130	0.004	9.596	0.018	...
0008	05 34 49.97	−05 18 44.6	12.583	0.004	11.496	0.010	10.928	0.010	10.474	0.004	9.616	0.023	108
0009	05 35 16.72	−05 23 25.2	9.928	0.021	10.075	0.026	10.122	0.012	9.908	0.006	9.652	0.019	...
0010	05 34 39.75	−05 24 25.6	14.065	0.004	12.535	0.010	11.606	0.008	10.906	0.003	9.794	0.021	45
...	...	...	...	...	...	...	...	...	...	...	...	...	...

Note. The Hα photometry is presented separately in Table 5. All the magnitudes are given the VegaMag instrumental system. The last column reports the corresponding ID of the source in the catalog of Hillenbrand (1997), if present.
(This table is available in its entirety in a machine-readable form in the online journal. A portion is shown here for guidance regarding its form and content.)

Our catalog, presenting for each star coordinates, calibrated magnitudes, and photometric errors in the U, B, V, I, and TiO bands, is given in Table 2 (including only photometry derived from night A observations, used in this work). We matched our catalog with the one of Hillenbrand (1997), and the last column of Table 2 reports (if present) the ID number of the latter.

In principle, the photometry from the second night could have been used to estimate the stellar variability and to provide a better characterization of the uncertainty associated to photometry. However, the poor seeing conditions of the second night strongly affect also the accuracy of the photometry. This is because in a field like the Orion Nebula source confusion and nonuniformity of the nebular background have a stronger influence on the photometric accuracy when the PSF is larger. If we limit ourselves to the brightest part of the photometric catalog, where these uncertainties have lower impact, we see that the standard deviation of the difference in magnitudes between the two nights, for the bright 50% of the population, is 0.17 mag in the I band, 0.30 mag in the V band and B band, 0.35 mag in the U band, on a time baseline of about 24 hr. This is compatible with what is found by Herbst et al. (2002), who report that more than 50% of the cluster members display a I-band variability larger than 0.2 mag over periods of a few days.

The reported coordinates are the positions measured on the reduced images in the I band, whose field distortion has been corrected by means of a polynomial warping using the 2MASS astrometry as a reference for all the matched sources. We estimate the precision of our astrometry comparing our positions with those of the H97 catalog and with the *HST*/ACS photometry. In the comparison with H97, the standard deviation of the coordinate offsets is 0.″24 in R.A. and 0.″22 in decl., while with respect to the *HST* photometry they decrease to 0.″13 and 0.″11, respectively. Given that the astrometric precision of the ACS catalog is much less than 1 pixel (0.″05), the latter dispersions are a good estimate of the uncertainty of our astrometry. Therefore, we consider the astrometric precision of our WFI catalog to be $\sim$0.″13, which therefore improves by a factor of 2 over H97.

The Hα catalog, expressed in terms of nonphotospheric flux excess, is presented independently (see Section 4.3).

It is worthwhile to estimate the improvement in the optical characterization of ONC stars of our sample with respect to the one of H97. The two catalogs cover a similar extension on the sky, but the latter, counting 1576 sources with respect to our 2621 stars, is centered on the Trapezium cluster whereas our observations are centered about 6′ to the southwest. If we consider only stars detected in the common area of the two catalogs, we have 2246 stars from WFI data and 1463 from H97, 926 of which are with known spectral types. We highlight that in the presented catalog we do not recover all the H97 sources in the common area, but we lose about 90 stars. This is mostly due for saturation in the WFI observations, but we also found for small sparse groups of stars evidence of systematic shifts in the coordinates between our coordinates and the H97 ones, large enough to fail our matching algorithms and probably due to erroneous coordinates in the literature. We do not consider those stars among the matched ones (the last column of Table 2)

4.2. The TiO Spectrophotometric Index

The depth of the TiO spectral feature shown in Figure 1 can be used to classify late-type stars. To this purpose, we have defined an index, [TiO], using the V, I, and TiO luminosities.

Our [TiO] index represents, roughly speaking, the "lack" of flux, in magnitudes, measured in the TiO feature, and is defined as the difference between the linear interpolation at 6200 Å of the V and I magnitudes and the apparent magnitude in the TiO band:

$$[\mathrm{TiO}] = m_{\mathrm{TiO,interp}} - m_{\mathrm{TiO}} = \left(V_{\mathrm{WFI}} - (V-I)_{\mathrm{WFI}} \cdot \frac{\lambda_{\mathrm{TiO}} - \lambda_V}{\lambda_I - \lambda_V}\right) - m_{\mathrm{TiO}} \quad (1)$$

where λ_V, λ_I, and λ_{TiO} are the central wavelengths of the three filters, as reported in Table 1.

In Figure 9 we plot our [TiO] index versus the spectral type extracted for all the stars available from Hillenbrand (1997). This sample counts 583 stars. For M-type stars, the depth of the TiO feature measured by means of narrowband photometry increases moving toward higher types, and is up to one magnitude fainter than the linear interpolation between V and I. In this spectral range, therefore, there is a definite correlation between [TiO] and spectral type, whereas for earlier classes it assumes a roughly constant value of $\simeq$ 0.1–0.2 mag. This limits its use to M-type stars and possibly brown dwarfs, which are not included in the H97 list.

By isolating within our catalog the stars with small photometric errors ($\Delta m_{\mathrm{TiO}} < 0.03$), we derived a quantitative relation between the TiO index and spectral type, extracted a moving

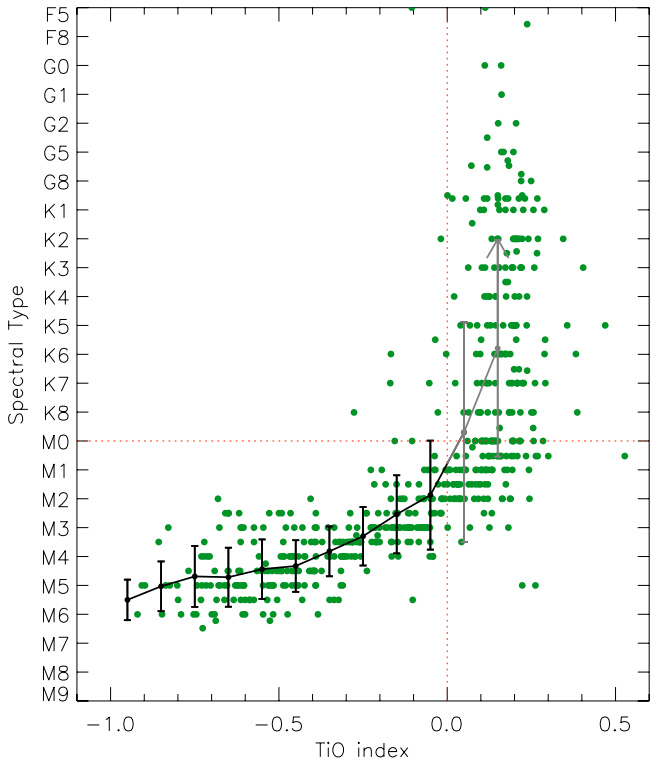

Figure 9. Spectral type vs. [TiO] index relation showing all the 583 stars for which H97 spectral types and TiO photometric index are available, 298 of which are with [TiO] < 0. The law we derived for M-type stars with low photometric errors ($\Delta m_{\rm TiO} \leqslant 0.03$) is overplotted (black line).

(A color version of this figure is available in the online journal.)

Table 3
Empirical TiO vs. Spectral Type Relation

TiO index	Sp Type	σ [types]
−0.95	M5.5	0.7
−0.85	M5.0	0.9
−0.75	M4.7	1.1
−0.65	M4.7	1.0
−0.55	M4.4	1.0
−0.45	M4.3	0.9
−0.35	M3.8	0.9
−0.25	M3.3	1.0
−0.15	M2.5	1.4
−0.05	M1.9	1.9
0.05	< M3.5	...
0.15	< M0.5	...

average, as shown in Figure 9, and shown in Table 3. The 1σ uncertainty is also reported, showing that our relation is accurate to better than 1 spectral subclass for M3-M6 types and better than 2 spectral subclasses for M0-M2 types.

We investigated the sources of scatter evident in the figure looking for dependences on other parameters. While assuming equal metallicity for the ONC members is quite legitimate, an age spread for the ONC members leads to a distribution of surface gravity for stars of a given mass, given that the stellar radius changes during PMS evolution. Specifically, we consider the tabulated values of $\log g$ derived in Hillenbrand (1997) using D'Antona & Mazzitelli (1994) evolutionary models on their H-R diagram. The latter was obtained from spectral types converted into $T_{\rm err}$ according to Cohen & Kuhi (1979) and bolometric corrections applied to reddening corrected $V-I$ photometry. In Figure 10 we present the surface gravity distribution, and

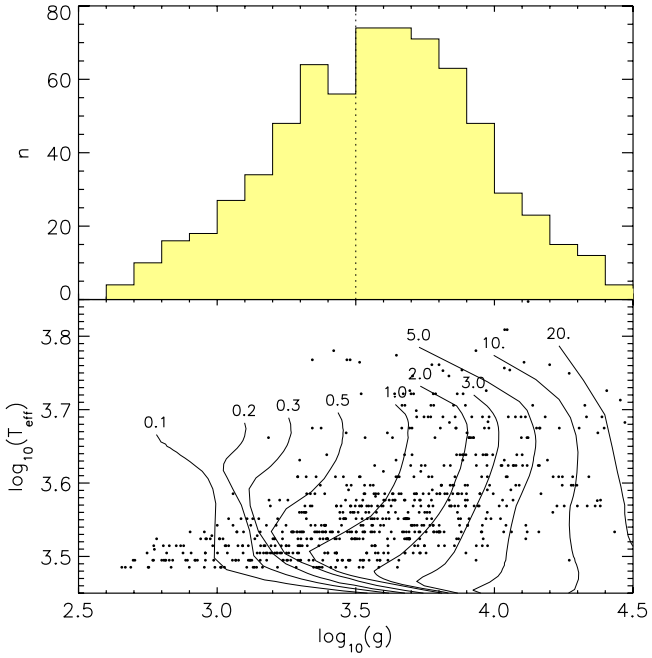

Figure 10. Upper panel: the distribution of $\log g$ (cgs units) from Hillenbrand (1997), limited to the sample of stars used to derive our [TiO]–spectral type relation. Lower panel: $T_{\rm eff}$ vs. $\log g$ from the same work. Isochrones from 0.1 Myr to 20 Myr from evolutionary models of D'Antona & Mazzitelli (1994) are overlaid, highlighting that the derived broad distribution of $\log g$ comes from the interpretation of the H–R diagram spread as due to an age distribution.

(A color version of this figure is available in the online journal.)

presenting the H97 stars in the $T_{\rm eff}$ versus $\log g$ in comparison with PMS isochrones of different ages, we show that the measured age spread in the ONC is the main cause of a wide distribution of surface gravity in our sample.

We divided our stars into two samples, of low and high surface gravity, and we found that variations in surface gravity introduce a systematic offset in the TiO index versus spectral type relation. In Figure 11 we show the result of isolating stars with $\log g < 3.5$ and $\log g > 3.5$ in cgs units (the threshold being the average value of $\log g$ in our sample). We subtracted the "predicted" spectral type from the [TiO] index using our law tabulated in Table 3 to the "actual" one, and for each of the two subsamples we computed the average of these residuals (Figure 11, bottom panel). This is not zero in the two cases, suggesting a real dependence of the behavior of our index on the stellar surface gravity.

We then carried out a statistical test of the average of two subsets, assuming a Gaussian distribution, and comparing the shift between the two mean values from zero with the relative rms. In other words, we computed the probability P that the two distributions are statistical representations of the same distribution considering the estimator z as follows:

$$z = \frac{m_1 - m_2}{\sqrt{\frac{\sigma_1^2}{N_1} + \frac{\sigma_2^2}{N_2}}} \quad (2)$$

where $m_1 - m_2 = 1.1$ spectral subtypes is the difference between the two mean values (shown in Figure 11(b) by the dashed and dotted lines), σ_1 and σ_2 are the standard deviations of the two sets, and N_1 and N_2 are the total number of stars in each set. We derived $z = 5.9$, corresponding to a probability (for the Gaussian hypothesis) of about 2×10^{-9}. This proves that the behavior of the TiO index is dependent on surface gravity, and,

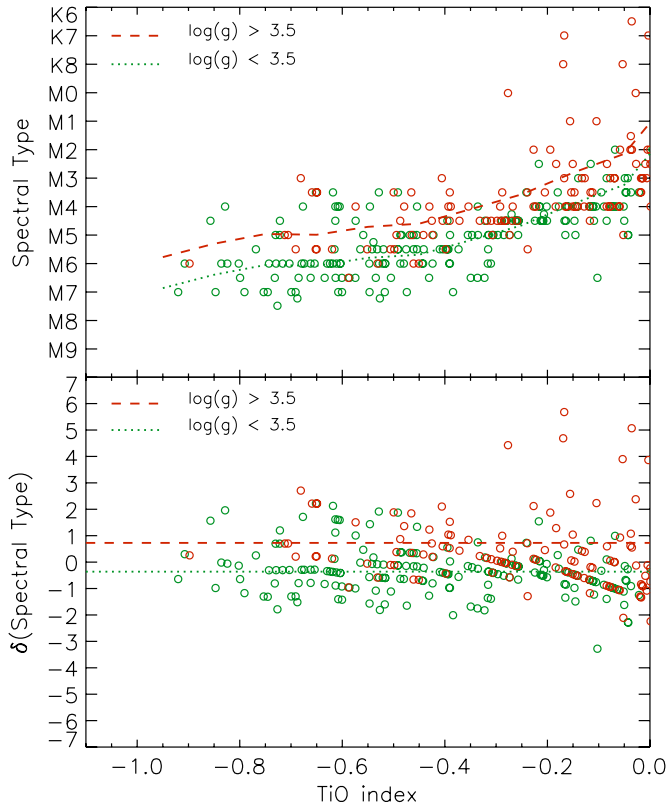

Figure 11. Upper panel: the relation for values of TiO indices for the cases of $\log g > 3.5$ and < 3.5 in cgs units. Bottom panel: the displacement in units of spectral types with respect to the global dependence of Table 3, showing the average in the two cases.

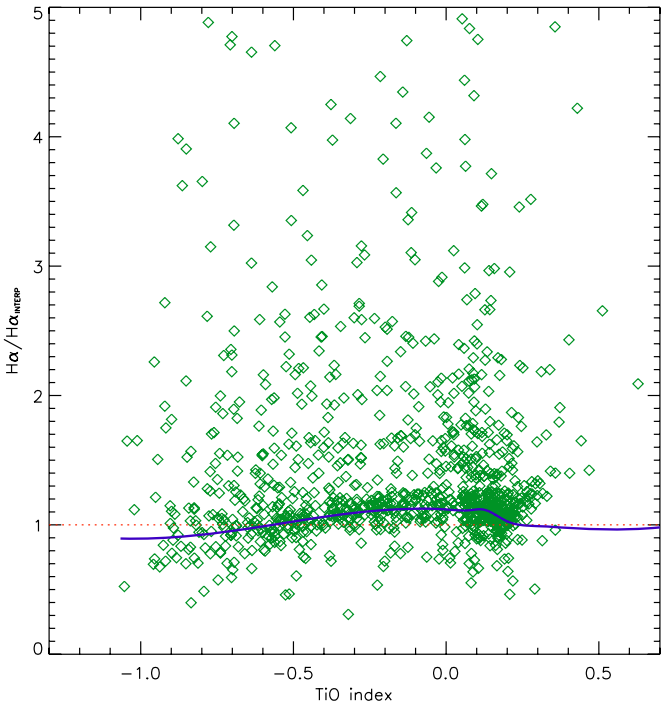

Figure 12. Ratio between the measured flux in Hα and the one interpolated between V and I, with respect to the [TiO] index. Although it is almost equal to unity for a significant fraction of stars that do not show excess (which means that the $V-I$ interpolation at 6563 Å is a good approximation for the intrinsic photospheric flux at this wavelength), the TiO index—and its correlation with spectral type—can be used to refine the level of intrinsic stellar flux. The thick solid line, obtained iterating a sigma-clipping robust mean computation technique, represents the zero-emission level at Hα as a function of the TiO index.

for a given value of the index, the higher the surface gravity, the lower is the derived spectral type. The difference between the averages of $\log g$ in the two subsets is equal to 0.53 dex. We derive a shift in the [TiO] versus $\log T_{\rm eff}$ relation of 2 subtypes per unit of $\log g$ with respect to our empirical law tabulated in Table 3, valid for the average value $\log g = 3.5$.

The dependence of the [TiO] index on surface gravity is intriguing, but its interpretation is not necessarily trivial. In fact, as the depth of the TiO feature is influenced by stellar surface gravity, for cold stars also the V and I band fluxes depend on the luminosity class, and therefore on the stellar parameter $\log g$. Moreover, the younger is a low-mass PMS star, the lower is its surface gravity (because of its larger radius); the dependence we found could be, therefore, introduced by different ages in the considered mass range. For instance, mass accretion, which is typically higher for young PMS objects, introduces veiling in the stellar spectrum, which decreases the relative depth of the spectral absorption features, causing a star of a given temperature to have a shallower TiO feature at younger ages.

In any case, neither age nor surface gravity is known for stars of the ONC for which the spectral type is not determined. This implies that using our [TiO]–spectral type relation to classify M-type stars cannot be refined by the aforementioned consideration about surface gravity. Therefore, we leave a detailed analysis of the sources of this effect in the [TiO] index to a future paper, considering, for the moment, only the global relation expressed in Table 3.

Using this, we compute the value of [TiO] for all stars not included in the H97 spectral catalog for which our V, I, and TiO band photometry is available. Selecting only sources with [TiO]< 0, we derive the spectral type and its uncertainty for 217 additional stars. The results are tabulated in Table 4.

4.3. The Hα Photometry

T Tauri stars are known to exhibit strong Hα emission, associated, together with UV excess, with ongoing mass accretion from a circumstellar disk to the star. The Hα excess is the most used observational quantity to estimate the mass accretion rates, an important parameter for understanding the evolution of both stars and disks. Here we describe the derived line excess derived from our photometry in the WFI Hα filter.

After having calibrated the Hα photometry into units of Jy, as described in Section 3.2.2, we derive the line excess, following an approach analogous to the one used for the TiO index. We computed the flux at 6563 Å by linear interpolation between the (logarithmic) fluxes in V and I. We computed for all stars the ratio between the measured flux and the interpolated flux; for stars that do not emit in Hα—or for which the line emission is negligible—this ratio should be close to unity. We analyzed the behavior of our assumption of linear interpolation for the photospheric flux by plotting the Hα excess as a function of the TiO index to highlight eventual trends with spectral class. In other words, it is reasonable to question the hypothesis that a relation of type ($V-I$) versus (6563 Å-I) is linear along the entire range in colors, especially for late-type stars.

Indeed, as seen in Figure 12, besides the presence of a large population of stars with a noticeable excess, all the stars without emission lie on a locus which has a weak, but definite, dependence on the TiO index, and therefore on spectral type

Table 4
New M-type Stars Classified from the [TiO] Index

	ID[a]	R.A. (J2000.0)	Decl. (J2000.0)	[TiO] (mag)	Spectral Type	σ
1	1306	05 36 00.49	−05 41 10.9	−0.145	M2.5	1.4
2	608	05 35 59.48	−05 37 09.6	−0.478	M4.4	0.9
3	1642	05 35 59.25	−05 33 00.4	−0.541	M4.4	1.0
4	630	05 35 57.51	−05 39 51.3	−0.080	M2.1	1.7
5	1571	05 35 57.35	−05 25 15.6	−0.457	M4.3	0.9
6	758	05 35 55.97	−05 42 26.3	−0.225	M3.1	1.1
7	1084	05 35 54.49	−05 26 45.6	−0.241	M3.2	1.0
8	1370	05 35 52.90	−05 25 43.9	−0.068	M2.0	1.8
9	732	05 35 52.20	−05 39 24.7	−0.001	M0.8	2.8
10	746	05 35 51.76	−05 17 39.4	−0.393	M4.0	0.9
11	815	05 35 48.71	−05 42 14.4	−0.369	M3.9	0.9
12	660	05 35 47.65	−05 37 38.8	−0.322	M3.7	0.9
13	304	05 35 46.42	−05 41 00.7	−0.400	M4.1	0.9
14	1233	05 35 44.58	−05 32 55.9	−0.321	M3.7	0.9
15	515	05 35 43.44	−05 40 55.0	−0.049	M1.9	1.9
16	938	05 35 42.66	−05 40 42.2	−0.462	M4.3	0.9
17	1404	05 35 42.61	−05 26 33.7	−0.550	M4.4	1.0
18	778	05 35 41.30	−05 38 32.9	−0.382	M4.0	0.9
19	890	05 35 41.23	−05 38 29.4	−0.410	M4.1	0.9
20	999	05 35 41.13	−05 42 51.1	−0.472	M4.4	0.9
21	379	05 35 40.83	−05 32 01.8	−0.311	M3.6	0.9
22	1258	05 35 37.06	−05 37 37.2	−0.569	M4.5	1.0
23	1390	05 35 36.55	−05 40 25.1	−0.510	M4.4	1.0
24	562	05 35 36.35	−05 31 37.8	−0.461	M4.3	0.9
25	629	05 35 35.95	−05 38 42.7	−0.334	M3.7	0.9
26	594	05 35 35.61	−05 29 36.5	−0.492	M4.4	1.0
27	549	05 35 35.14	−05 21 23.6	−0.115	M2.3	1.5
28	1271	05 35 35.02	−05 41 01.4	−0.307	M3.6	0.9
29	1322	05 35 34.64	−05 27 15.0	−0.692	M4.7	1.0
30	1038	05 35 34.61	−05 15 52.7	−0.442	M4.3	0.9
31	879	05 35 34.37	−05 26 59.6	−0.814	M4.9	0.9
32	293	05 35 34.21	−05 27 18.2	−0.334	M3.7	0.9
33	947	05 35 33.59	−05 15 23.2	−0.045	M1.8	2.0
34	734	05 35 33.41	−05 39 21.3	−0.186	M2.8	1.2
35	545	05 35 33.31	−05 39 24.9	−0.086	M2.1	1.7
36	664	05 35 33.11	−05 17 34.0	−0.525	M4.4	1.0
37	1313	05 35 32.88	−05 39 19.1	−0.748	M4.7	1.1
38	1459	05 35 32.60	−05 40 12.4	−0.684	M4.7	1.0
39	1116	05 35 31.75	−05 16 39.9	−0.038	M1.6	2.1
40	838	05 35 31.68	−05 42 46.0	−0.239	M3.2	1.1
41	814	05 35 31.56	−05 16 36.9	−0.978	M5.6	0.7
42	1108	05 35 31.53	−05 15 23.6	−0.140	M2.5	1.4
43	657	05 35 30.70	−05 18 07.1	−0.050	M1.9	1.9
44	1011	05 35 30.63	−05 15 16.3	−0.789	M4.8	1.0
45	460	05 35 30.42	−05 34 38.6	−0.564	M4.5	1.0
46	364	05 35 29.80	−05 16 06.4	−0.038	M1.6	2.1
47	1517	05 35 29.67	−05 30 24.7	−0.301	M3.6	0.9
48	794	05 35 28.77	−05 41 34.0	−0.230	M3.1	1.1
49	1009	05 35 28.28	−05 37 19.6	−0.644	M4.7	1.0
50	487	05 35 27.66	−05 42 55.2	−0.307	M3.6	0.9
51	432	05 35 27.20	−05 30 24.7	−0.518	M4.4	1.0
52	638	05 35 26.72	−05 16 45.1	−0.405	M4.1	0.9
53	780	05 35 26.45	−05 30 16.4	−0.358	M3.9	0.9
54	939	05 35 25.53	−05 34 04.7	−0.067	M2.0	1.8
55	823	05 35 25.33	−05 25 29.4	−0.354	M3.8	0.9
56	725	05 35 25.22	−05 29 51.6	−0.461	M4.3	0.9
57	284	05 35 24.64	−05 11 58.3	−0.253	M3.3	1.0
58	484	05 35 24.47	−05 11 58.0	−0.469	M4.3	0.9
59	644	05 35 24.09	−05 21 32.7	−0.499	M4.4	1.0
60	948	05 35 23.50	−05 34 23.4	−0.435	M4.3	0.9
61	1054	05 35 22.68	−05 16 14.0	−0.072	M2.0	1.8
62	341	05 35 22.61	−05 14 11.2	−0.143	M2.5	1.4
63	1015	05 35 22.24	−05 18 08.8	−0.735	M4.7	1.0
64	1337	05 35 22.07	−05 28 55.6	−0.341	M3.8	0.9
65	667	05 35 21.97	−05 17 04.9	−0.560	M4.5	1.0

Table 4
(Continued)

	ID[a]	R.A. (J2000.0)	Decl. (J2000.0)	[TiO] (mag)	Spectral Type	σ
66	743	05 35 21.88	−05 17 03.4	−0.428	M4.2	0.9
67	1347	05 35 21.63	−05 17 19.1	−0.288	M3.5	1.0
68	713	05 35 21.62	−05 26 57.5	−0.474	M4.4	0.9
69	560	05 35 21.62	−05 34 58.4	−0.333	M3.7	0.9
70	420	05 35 21.25	−05 42 12.3	−0.151	M2.5	1.3
71	795	05 35 21.15	−05 18 21.3	−0.378	M4.0	0.9
72	415	05 35 20.93	−05 40 14.3	−0.521	M4.4	1.0
73	739	05 35 20.56	−05 20 43.2	−0.084	M2.1	1.7
74	1314	05 35 19.86	−05 31 03.7	−0.178	M2.8	1.3
75	770	05 35 19.81	−05 22 21.6	−0.084	M2.1	1.7
76	491	05 35 19.79	−05 30 37.5	−0.563	M4.5	1.0
77	836	05 35 19.75	−05 39 35.6	−0.235	M3.2	1.1
78	1246	05 35 19.56	−05 27 35.6	−0.030	M1.4	2.3
79	408	05 35 19.48	−05 36 51.8	−0.276	M3.4	1.0
80	1486	05 35 19.32	−05 16 09.9	−0.198	M2.9	1.2
81	414	05 35 18.83	−05 14 45.6	−0.211	M3.0	1.1
82	1185	05 35 18.49	−05 42 30.7	−0.516	M4.4	1.0
83	1104	05 35 18.46	−05 39 19.8	−0.522	M4.4	1.0
84	454	05 35 18.29	−05 28 46.1	−0.143	M2.5	1.4
85	1070	05 35 17.97	−05 16 45.1	−0.095	M2.2	1.6
86	523	05 35 17.93	−05 25 33.8	−0.186	M2.8	1.2
87	666	05 35 17.66	−05 23 41.0	−1.033	M5.9	0.6
88	433	05 35 17.53	−05 40 48.3	−0.248	M3.3	1.0
89	552	05 35 17.43	−05 30 25.3	−0.119	M2.3	1.5
90	468	05 35 17.34	−05 42 14.6	−0.076	M2.0	1.7
91	707	05 35 17.15	−05 41 53.8	−0.492	M4.4	1.0
92	723	05 35 17.00	−05 15 44.2	−0.396	M4.1	0.9
93	950	05 35 16.81	−05 39 17.0	−0.582	M4.5	1.0
94	68	05 35 16.75	−05 24 04.2	−0.007	M0.9	2.7
95	686	05 35 15.95	−05 16 57.5	−0.222	M3.1	1.1
96	709	05 35 15.94	−05 41 11.4	−0.441	M4.3	0.9
97	1588	05 35 15.49	−05 22 42.9	−0.048	M1.8	1.9
98	642	05 35 15.48	−05 35 11.9	−0.157	M2.6	1.3
99	375	05 35 15.30	−05 39 56.1	−0.329	M3.7	0.9
100	936	05 35 14.63	−05 16 46.1	−0.510	M4.4	1.0
101	912	05 35 13.75	−05 34 54.9	−0.401	M4.1	0.9
102	576	05 35 13.65	−05 28 46.2	−0.189	M2.8	1.2
103	693	05 35 13.56	−05 27 57.2	−0.482	M4.4	0.9
104	1130	05 35 13.31	−05 37 15.8	−0.792	M4.8	1.0
105	1274	05 35 13.17	−05 36 18.0	−0.218	M3.1	1.1
106	1078	05 35 12.94	−05 28 49.8	−0.241	M3.2	1.0
107	1648	05 35 12.40	−05 24 03.7	−0.317	M3.6	0.9
108	681	05 35 12.26	−05 20 45.2	−0.246	M3.3	1.0
109	917	05 35 12.04	−05 14 14.6	−0.179	M2.8	1.3
110	662	05 35 11.77	−05 21 55.5	−0.470	M4.4	0.9
111	942	05 35 11.72	−05 23 51.9	−0.471	M4.4	0.9
112	706	05 35 11.65	−05 31 01.1	−0.485	M4.4	0.9
113	1222	05 35 11.23	−05 41 36.1	−0.191	M2.8	1.2
114	721	05 35 11.17	−05 19 35.8	−0.397	M4.1	0.9
115	1168	05 35 11.07	−05 41 56.3	−0.624	M4.6	1.0
116	915	05 35 10.90	−05 22 46.4	−0.169	M2.7	1.3
117	984	05 35 10.41	−05 19 52.4	−0.186	M2.8	1.2
118	482	05 35 10.13	−05 22 32.6	−0.056	M1.9	1.9
119	808	05 35 09.27	−05 16 56.0	−0.098	M2.2	1.6
120	690	05 35 08.29	−05 24 34.9	−0.613	M4.6	1.0
121	827	05 35 08.03	−05 36 14.1	−0.628	M4.7	1.0
122	1272	05 35 07.09	−05 42 33.3	−0.299	M3.6	0.9
123	941	05 35 06.91	−05 26 00.5	−0.722	M4.7	1.0
124	1064	05 35 06.83	−05 42 35.4	−0.283	M3.5	1.0
125	898	05 35 06.42	−05 27 04.7	−0.741	M4.7	1.1
126	1348	05 35 05.75	−05 35 22.1	−0.739	M4.7	1.0
127	413	05 35 05.69	−05 25 04.1	−0.346	M3.8	0.9
128	1123	05 35 05.67	−05 43 04.6	−0.594	M4.6	1.0
129	945	05 35 05.61	−05 18 24.8	−0.378	M4.0	0.9
130	513	05 35 05.13	−05 20 24.4	−0.130	M2.4	1.5

Table 4
(Continued)

	ID[a]	R.A. (J2000.0)	Decl. (J2000.0)	[TiO] (mag)	Spectral Type	σ
131	1753	05 35 03.79	−05 24 54.4	−0.435	M4.3	0.9
132	1403	05 35 02.99	−05 38 40.5	−0.613	M4.6	1.0
133	1209	05 35 02.69	−05 32 24.9	−0.597	M4.6	1.0
134	1150	05 35 01.71	−05 27 09.8	−0.802	M4.9	1.0
135	1035	05 35 01.32	−05 18 21.3	−0.436	M4.3	0.9
136	503	05 35 01.16	−05 29 55.2	−0.243	M3.2	1.0
137	1540	05 34 59.18	−05 41 12.5	−0.296	M3.5	0.9
138	1572	05 34 57.36	−05 32 43.1	−0.031	M1.5	2.3
139	522	05 34 57.23	−05 42 02.7	−0.052	M1.9	1.9
140	1152	05 34 53.48	−05 40 03.9	−0.525	M4.4	1.0
141	1603	05 34 53.07	−05 26 27.7	−0.619	M4.6	1.0
142	1224	05 34 52.67	−05 21 25.2	−0.395	M4.0	0.9
143	1067	05 34 52.36	−05 25 00.7	−0.940	M5.5	0.7
144	626	05 34 52.34	−05 30 07.9	−0.384	M4.0	0.9
145	331	05 34 51.74	−05 39 24.0	−0.106	M2.2	1.6
146	735	05 34 50.86	−05 39 29.2	−0.482	M4.4	0.9
147	1363	05 34 50.21	−05 35 39.0	−0.789	M4.8	1.0
148	1138	05 34 48.45	−05 31 07.2	−0.336	M3.7	0.9
149	1543	05 34 47.73	−05 26 32.1	−0.434	M4.2	0.9
150	1510	05 34 47.66	−05 31 11.7	−0.331	M3.7	0.9
151	1562	05 34 46.87	−05 30 19.7	−0.501	M4.4	1.0
152	481	05 34 45.87	−05 41 09.6	−0.212	M3.0	1.1
153	307	05 34 42.73	−05 28 37.5	−0.154	M2.6	1.3
154	1366	05 34 42.48	−05 22 46.2	−0.623	M4.6	1.0
155	1242	05 34 42.19	−05 33 03.5	−0.217	M3.0	1.1
156	1243	05 34 41.96	−05 21 32.0	−0.654	M4.7	1.0
157	1160	05 34 41.72	−05 36 48.7	−0.509	M4.4	1.0
158	1211	05 34 39.11	−05 34 02.3	−0.739	M4.7	1.0
159	969	05 34 38.19	−05 35 49.5	−0.437	M4.3	0.9
160	181	05 34 36.54	−05 36 17.1	−0.008	M1.0	2.7
161	661	05 34 35.76	−05 40 09.4	−0.155	M2.6	1.3
162	702	05 34 35.68	−05 35 52.1	−0.180	M2.8	1.3
163	1230	05 34 35.60	−05 37 24.0	−0.597	M4.6	1.0
164	655	05 34 33.72	−05 40 22.7	−0.595	M4.6	1.0
165	858	05 34 32.23	−05 41 48.4	−0.400	M4.1	0.9
166	1155	05 34 30.24	−05 17 01.2	−0.550	M4.4	1.0
167	1052	05 34 30.11	−05 40 15.2	−0.618	M4.6	1.0
168	979	05 34 29.34	−05 33 39.7	−0.128	M2.4	1.5
169	1121	05 34 28.96	−05 23 48.1	−0.636	M4.7	1.0
170	1391	05 34 28.56	−05 30 32.4	−0.409	M4.1	0.9
171	570	05 34 27.80	−05 42 10.2	−0.025	M1.3	2.4
172	401	05 34 27.53	−05 28 28.4	−0.425	M4.2	0.9
173	565	05 34 26.75	−05 41 57.3	−0.194	M2.9	1.2
174	995	05 34 25.78	−05 35 46.5	−0.411	M4.1	0.9
175	949	05 34 25.54	−05 37 02.3	−0.350	M3.8	0.9
176	907	05 34 24.05	−05 42 22.1	−0.295	M3.5	0.9
177	688	05 34 21.23	−05 35 34.7	−0.502	M4.4	1.0
178	902	05 34 18.68	−05 37 08.1	−0.451	M4.3	0.9
179	1708	05 34 18.37	−05 22 54.9	−0.297	M3.5	0.9
180	256	05 34 17.48	−05 31 58.6	−0.138	M2.5	1.4
181	525	05 34 17.43	−05 30 35.2	−0.189	M2.8	1.2
182	1418	05 34 17.26	−05 22 36.8	−0.022	M1.3	2.4
183	1489	05 34 17.15	−05 37 11.8	−0.269	M3.4	1.0
184	388	05 34 17.14	−05 38 16.8	−0.237	M3.2	1.1
185	1053	05 34 16.95	−05 30 53.2	−0.811	M4.9	0.9
186	1294	05 34 15.09	−05 23 00.0	−0.309	M3.6	0.9
187	615	05 34 13.87	−05 36 35.3	−0.479	M4.4	0.9
188	1017	05 34 13.51	−05 35 38.6	−0.050	M1.9	1.9
189	395	05 34 13.20	−05 33 53.5	−0.131	M2.4	1.5
190	889	05 34 12.71	−05 41 36.4	−0.446	M4.3	0.9
191	1086	05 34 12.33	−05 41 34.7	−0.489	M4.4	0.9
192	864	05 34 12.02	−05 24 19.6	−0.284	M3.5	1.0
193	1113	05 34 11.50	−05 30 19.8	−0.784	M4.8	1.0
194	457	05 34 09.01	−05 24 05.6	−0.065	M2.0	1.8
195	121	05 34 08.22	−05 11 43.0	−0.168	M2.7	1.3

Table 4
(Continued)

	ID[a]	R.A. (J2000.0)	Decl. (J2000.0)	[TiO] (mag)	Spectral Type	σ
196	641	05 34 07.96	−05 36 17.0	−0.288	M3.5	1.0
197	839	05 34 07.80	−05 22 32.3	−0.216	M3.0	1.1
198	358	05 34 07.46	−05 13 36.4	−0.139	M2.5	1.4
199	1099	05 34 07.22	−05 29 32.4	−0.636	M4.7	1.0
200	1032	05 34 07.13	−05 22 27.0	−0.778	M4.8	1.0
201	1073	05 34 07.12	−05 15 59.3	−0.357	M3.9	0.9
202	1457	05 34 07.02	−05 30 20.0	−0.322	M3.7	0.9
203	1090	05 34 06.86	−05 23 08.3	−0.808	M4.9	0.9
204	1508	05 34 06.78	−05 21 46.8	−0.472	M4.4	0.9
205	1057	05 34 04.64	−05 22 22.4	−0.357	M3.9	0.9
206	918	05 34 04.40	−05 36 26.4	−0.650	M4.7	1.0
207	1257	05 34 03.89	−05 29 51.1	−0.618	M4.6	1.0
208	480	05 34 03.71	−05 22 18.7	−0.236	M3.2	1.1
209	935	05 34 02.91	−05 39 21.1	−0.456	M4.3	0.9
210	1343	05 34 02.67	−05 33 02.9	−0.854	M5.1	0.9
211	647	05 33 57.91	−05 36 26.9	−0.284	M3.5	1.0
212	362	05 33 57.68	−05 40 06.0	−0.098	M2.2	1.6
213	427	05 33 56.77	−05 21 33.4	−0.410	M4.1	0.9
214	946	05 33 56.56	−05 39 04.3	−0.389	M4.0	0.9
215	1241	05 33 53.97	−05 27 34.5	−0.083	M2.1	1.7
216	553	05 33 53.08	−05 35 15.7	−0.471	M4.4	0.9
217	384	05 33 52.11	−05 30 28.3	−0.268	M3.4	1.0

Note. [a] IDs (second column) are as in Table 2.

(see the [TiO]–temperature relation described in Section 4.2). We isolated this curve iterating a sigma-clipping algorithm and considered this flux level as the photospheric baseline. Clearly this baseline is valid on a statistical base, given that the real photospheric flux in proximity of the Hα can have a small dependence on other stellar parameters besides the V and I magnitudes and the [TiO]-derived spectral type, but our estimate remains the best guess relying on our own data.

The line excess, in mJy, does not yet represent the true line emission of the stars, because the filter profile is not centered at $\lambda_{H\alpha}$ but is displaced 25 Å toward redder wavelengths, and at the line wavelength the filter throughput is about 80% of its peak. While for the photospheric baseline, locally constant, one can approximate the filter throughput as a squared profile, neglecting the true shape of the filter, this local variation of efficiency must be taken into account, increasing the flux excess by a factor of approximately 20%. We investigated the possibility that, in the case of a very broad Hα line in emission, part of the flux could end up in a part of the filter profile characterized by a very low transmission, limiting the accuracy of the correction factor we applied to the flux. However, CTTSs tend to have Hα line emissions with a relatively limited range of broadenings, usually not exceeding $\sim$ 200 km s^{-1} (4–5 Å) (e.g., Alencar & Basri 2000), much lower than the WFI Hα filter width. In Figure 13 we show the filter throughput as a function of wavelength with three examples of $H\alpha$ lines (assumed Gaussian for simplicity) overplotted, with a sigma of 100, 200, and 300 km s^{-1}. It is evident that, even for a relatively high line broadening, the fraction of line flux that ends up in a region of the filter characterized by a very low transparency is negligible, and that, within the line, the throughput can be considered quite linear. Therefore our assumption that the overall transparency of the filter for a Hα line in emission can be considered constant and independent of the line broadening is fairly good, or, at least, not the major source of uncertainty in this result.

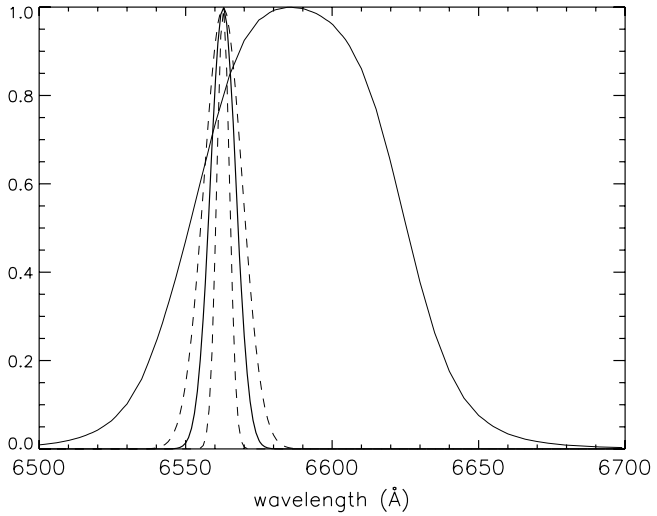

Figure 13. WFI Hα filter profile (broad solid line) is compared to Hα emission lines, assumed Gaussian for simplicity, of different widths: 200 km s^{-1} (thick solid line), 100 km s^{-1} and 300 km s^{-1} (dashed lines). The filter central wavelength is located about 25 Å to the red with respect to $\lambda_{H\alpha}$ = 6563 Å, where the transparency of the filter is about 80% of its peak. For a typical value of broadening for the Hα emission of CTTS of $\Delta\lambda \lesssim$ 200 km s^{-1} the, and therefore this average value of filter transparency can be reasonably considered independent of the line broadening.

We correct for this factor and present our the result in Table 5, reporting the excesses both in physical flux and in equivalent width (EW),[10] as well as the estimated photospheric continuum level.

In Figures 14 and 15 we present the sky distribution of the sources for which we detect an excess in the Hα flux. A

[10] For the equivalent width we follow the standard convention, i.e. positive EW is associated with an absorption, negative EW with an emission.

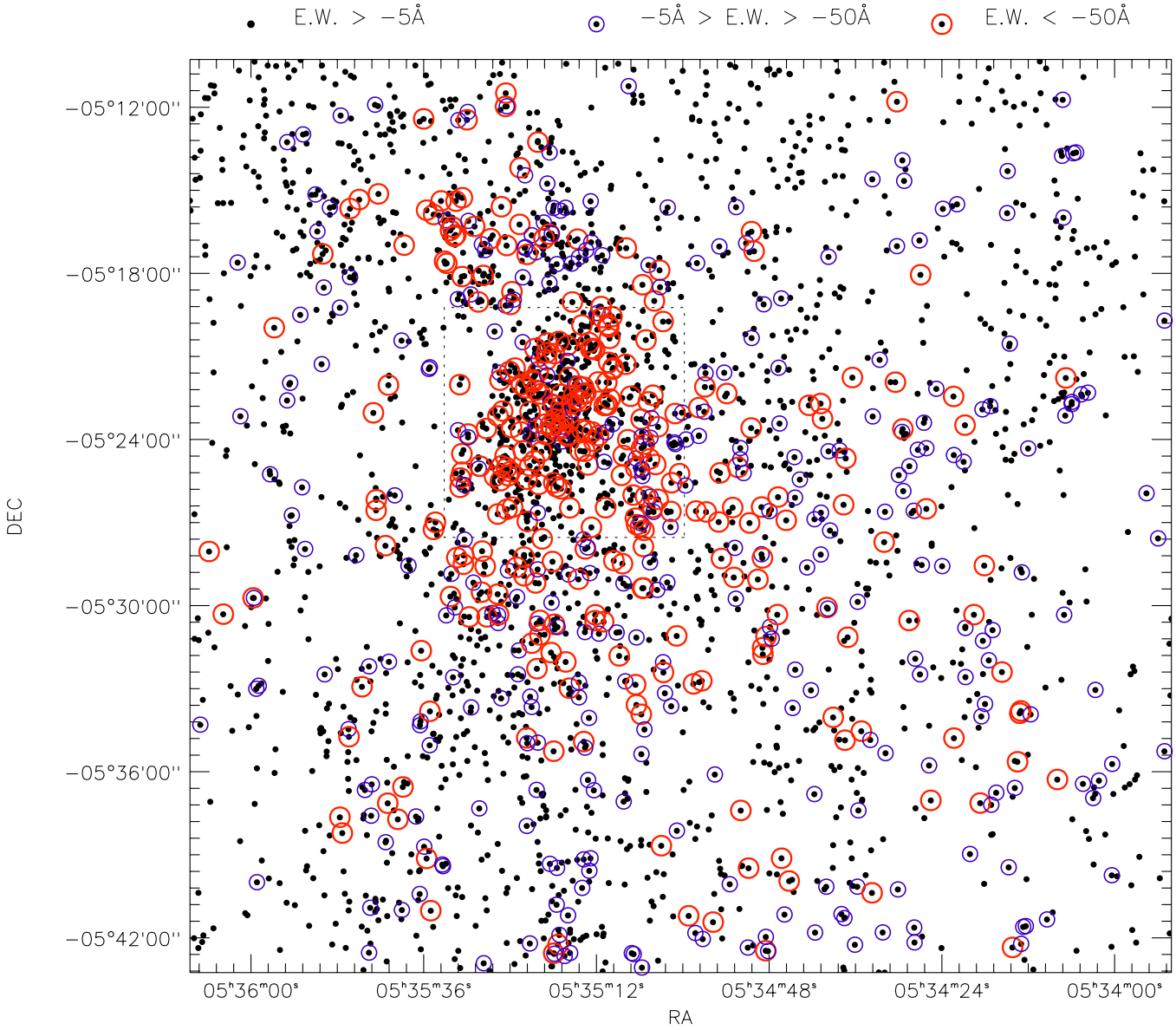

Figure 14. Distribution of the stars associated to a Hα excess. Black points have EW > −5 Å and represent absorption and very weak emission sources; 315 stars are characterized by a weak excess that we defined to be such that the measured equivalent width of the line emission (in absolute value) is between 5 Å and 50 Å(small blue circles), while 323 stars show a strong line excess, exceeding 50 Å in EW (large red circles).

Table 5
Hα Excess

	ID	R.A.	Decl.	EW		Hα excess		Hα cont.	
		(J2000)	(J2000)	(Å)	(Hz)	(erg s^{-1} cm^{-2})	(mJy)	(erg s^{-1} cm^{-2})	(mJy)
1	911	05 36 07.04	−05 34 18.3	−49.3	−3.43E+012	1.69E-014	0.317	2.63E-014	0.493
2	1219	05 36 05.82	−05 28 02.9	−114.	−7.94E+012	1.55E-014	0.290	1.04E-014	0.195
3	1136	05 36 05.75	−05 18 55.9	−1.84	−1.28E+011	3.10E-016	0.00582	1.29E-014	0.242
4	622	05 36 05.19	−05 21 34.5	6.83	4.75E+011	−2.12E-015	−0.0398	2.38E-014	0.446
5	832	05 36 03.85	−05 30 18.7	−108.	−7.50E+012	5.05E-014	0.948	3.59E-014	0.673
6	1298	05 36 03.47	−05 24 35.9	19.6	1.37E+012	−1.34E-015	−0.0251	5.22E-015	0.0980
7	909	05 36 03.36	−05 24 23.2	3.50	2.44E+011	−1.10E-015	−0.0206	2.40E-014	0.450
8	1111	05 36 02.82	−05 32 54.3	6.15	4.28E+011	−7.32E-016	−0.0137	9.12E-015	0.171
9	887	05 36 02.75	−05 15 27.1	−1.12	−7.79E+010	2.00E-016	0.00375	1.37E-014	0.256
10	1581	05 36 02.59	−05 34 31.3	9.48	6.60E+011	−4.59E-016	−0.00861	3.70E-015	0.0695
...	...	...	...	...	...	...	...	...	...

Note. IDs (second column) are as in Table 2.
(This table is available in its entirety in a machine-readable form in the online journal. A portion is shown here for guidance regarding its form and content.)

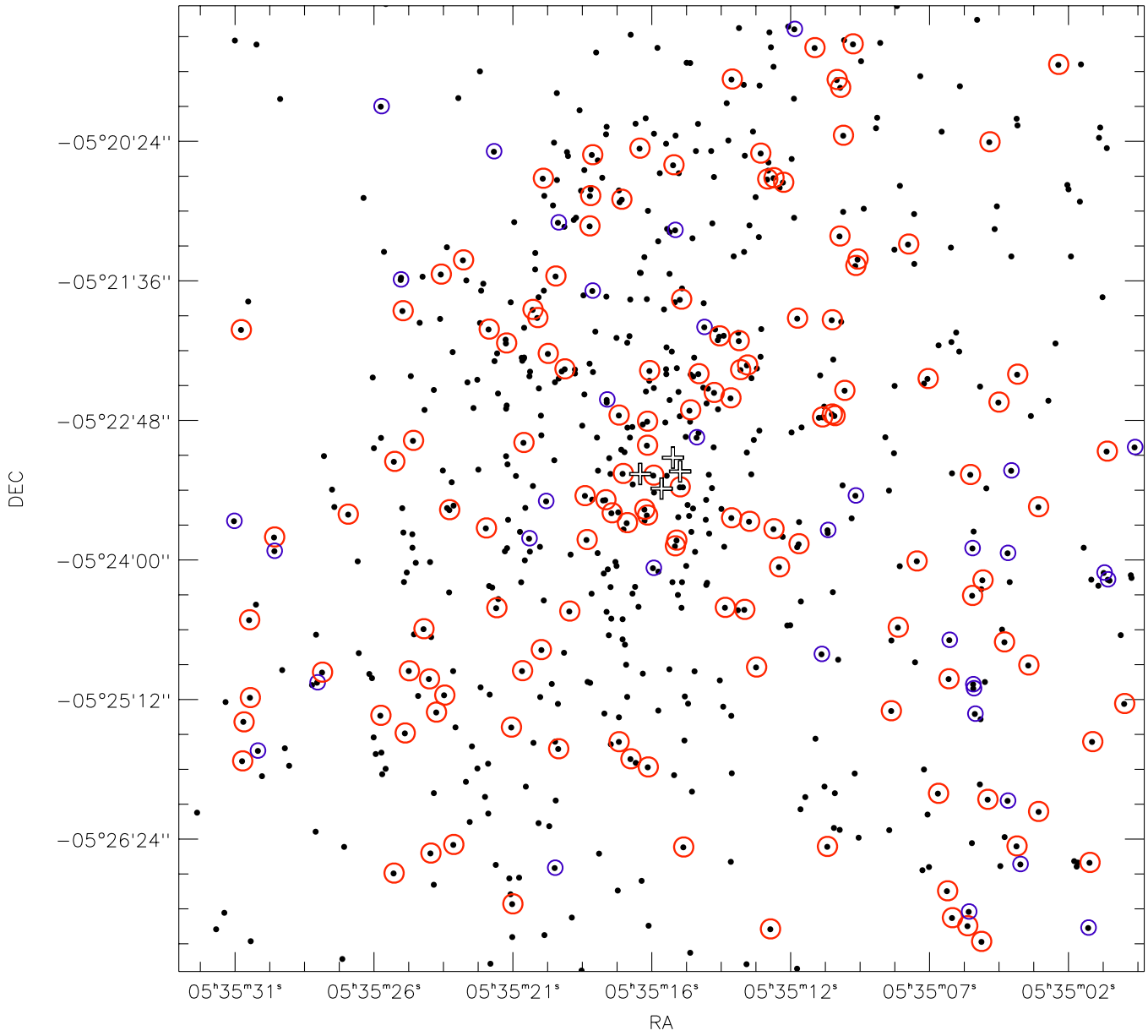

Figure 15. Same as Figure 15, for the inner (1 pc × 1 pc) part of the ONC, centered on the trapezium cluster (denoted by crosses).

remarkable number of these latter is characterized by a line excess with an equivalent width of more than 50 Å in modulus.

Unfortunately an accurate evaluation of the uncertainty in the derived Hα emission is limited. Presumably a fraction of the stars can suffer from strong nebular Hα contamination due to the nonuniformity of the latter and the relatively low spatial resolution of the seeing limited ground-based observations. Furthermore, emission from unresolved photoevaporated circumstellar disks can lead to an overestimate of the Hα excess. A qualitative estimate of at least the first bias is possible from the observed scatter in the ratio between the observed flux and the interpolated continuum level for the stars that do not show line excess. For this purpose we considered all the stars with a positive EW (i.e., Hα absorption; these are the points of Figure 12 located below the locus where nonemitters should lie (thick line). In an ideal case they should be characterized by a EW$\simeq$ 0; however, their scatter, which presents a standard deviation of 12% and a distribution with tails extended to 50% of the predicted continuum level, can be considered as representative of the overall uncertainty that we associate with the measured excess. A better estimate of the latter will be possible by means of a cross matching with the photometry obtained with the *HST*/ACS catalog, for all the sources in the common area, which we postpone to a future publication of our group.

These results will be used, together with the ultraviolet excess obtainable from our WFI *U*-band photometry, to study the mass accretion rates.

5. SUMMARY

In this work we present a set of ground-based, simultaneous, broadband observations of the Orion Nebula Cluster. We produce a catalog in the *U B*, *V*, *I*, TiO ($\sim$6200 Å) and Hα bands with the Wide Field Imager at the 2.2 m telescope at LaSilla. We publish the calibrated photometry in the WFI instrumental photometric system, corrected for zero point according to the VegaMag standard for the first five bands. The choice of not converting our data into standard systems (such as, for instance,

the Johnson–Cousins) is required by the significant diversity of the WFI filter bandpasses, which would require high color term corrections, limiting the accuracy of the transformation because of the dependence of these transformations on stellar parameters. As we are going to show in the second part of this work, this does not affect, by any means, the practicality of a thorough analysis of our photometric data set in order to study the PMS population of the ONC.

We define a spectrophotometric index, which we name the [TiO] index, from the fluxes in *V*, *I*, and TiO 6200 Å, and, comparing it with the spectral atlas of ONC members of Hillenbrand (1997), we find and present a correlation between the two quantities in the M-type stars range. This allows us to classify 217 new stars, whose spectral type is now presented.

We present the Hα photometry, calibrated in terms of energy flux, and, evaluating in a rigorous way the intrinsic photospheric contribution in the luminosity at the Hα wavelength, we derive the line excess. We present therefore the Hα excess in terms of equivalent width or physical flux for 1040 stars of our catalog, and we discuss the accuracy of the reported values. These latter will be used to derive and study the mass accretion rates in the Orion Nebula Cluster.

We thank ESO's General Director for awarding DDT time to this project and the ESO staff in La Silla for carrying out the observations in Service Observing mode. We acknowledge the European Southern Observatory for the use of the software *alambic* (ESO/MVM).

This work was made possible in part by GO program 10246 of the *Hubble Space Telescope*, which is operated by the Space Telescope Science Institute.

This work was made possible through the Summer Student Program of the Space Telescope Science Institute.

Facilities: ESO

REFERENCES

Ali, B., & Depoy, D. L. 1995, AJ, 109, 709
Alencar, S. H. P., & Basri, G. 2000, AJ, 119, 1881
Baraffe, I., Chabrier, G., Allard, F., & Hauschildt, P. H. 1998, A&A, 337, 403
Bertin, E., Mellier, Y., Radovich, M., Missonnier, G., Didelon, P., & Morin, B. 2002, in ASP Conf. Ser. 281, Astronomical Data Analysis Software and Systems XI, ed. D. A. Bohlender, D. Durand, & T. H. Handley (San Francisco, CA: ASP), 228
Cohen, M., & Kuhi, L. V. 1979, ApJS, 41, 743
D'Antona, F., & Mazzitelli, I. 1994, ApJS, 90, 467
Getman, K. V., Feigelson, E. D., Grosso, N., McCaughrean, M. J., Micela, G., Broos, P., Garmire, G., & Townsley, L. 2005, ApJS, 160, 353
Gunn, J. E., & Stryker, L. L. 1983, ApJS, 52, 121
Hauschildt, P. H., Allard, F., & Baron, E. 1999, ApJ, 512, 377
Herbig, G. H., & Terndrup, D. M. 1986, ApJ, 307, 609
Herbst, W., Bailer-Jones, C. A. L., Mundt, R., Meisenheimer, K., & Wackermann, R. 2002, A&A, 396, 513
Hillenbrand, L. A. 1997, AJ, 113, 1733 (H97)
Hillenbrand, L. A., & Carpenter, J. M. 2000, ApJ, 540, 236
Hillenbrand, L. A., & Hartmann, L. W. 1998, ApJ, 492, 540
Hillenbrand, L. A., Strom, S. E., Calvet, N., Merrill, K. M., Gatley, I., Makidon, R. B., Meyer, M. R., & Skrutskie, M. F. 1998, AJ, 116, 1816
Jones, B. F., & Walker, M. F. 1988, AJ, 95, 1755
Lada, C. J., & Lada, E. A. 2003, ARA&A, 41, 57
Landolt, A. U. 1992, AJ, 104, 340
Lucas, P. W., & Roche, P. F. 2000, MNRAS, 314, 858
Luhman, K. L., Rieke, G. H., Young, E. T., Cotera, A. S., Chen, H., Rieke, M. J., Schneider, G., & Thompson, R. I. 2000, ApJ, 540, 1016
Maíz-Apellániz, J. 2004, PASP, 116, 859
Menten, K. M., Reid, M. J., Forbrich, J., & Brunthaler, A. 2007, A&A, 474, 515
Prosser, C. F., Stauffer, J. R., Hartmann, L., Soderblom, D. R., Jones, B. F., Werner, M. W., & McCaughrean, M. J. 1994, ApJ, 421, 517
Robberto, M., Song, J., Mora Carrillo, G., Beckwith, S. V. W., Makidon, R. B., & Panagia, N. 2004, ApJ, 606, 952
Robberto, M., et al. 2005, AJ, 129, 1534
Slesnick, C. L., Hillenbrand, L. A., & Carpenter, J. M. 2004, ApJ, 610, 1045
Smith, N., Bally, J., Shuping, R. Y., Morris, M., & Kassis, M. 2005, AJ, 130, 1763
Stetson, P. B. 1987, PASP, 99, 191
Vandame, B. 2004, PhD thesis, Nice Univ.